Manganese containing copper aluminate catalysts

Dörfelt, Christoph; Hammerton, Michelle; Martin, David; Wellmann, Alexander; Aletsee, Clara C.; Tromp, Moniek; Köhler, Klaus

Published in:
Journal of Catalysis

DOI:
10.1016/j.jcat.2020.12.017

Publication date:
2021

Journal of Catalysis 395 (2021) 80–90

Contents lists available at ScienceDirect

Journal of Catalysis

journal homepage: www.elsevier.com/locate/jcat

Manganese containing copper aluminate catalysts: Genesis of structures and active sites for hydrogenation of aldehydes

Christoph Dörfelt [a,d,1], Michelle Hammerton [b,1], David Martin [b], Alexander Wellmann [a], Clara C. Aletsee [a], Moniek Tromp [b,c,*], Klaus Köhler [a,*]

[a] Department of Chemistry, Inorganic Chemistry, Lichtenbergstrasse 4 and Catalysis Research Center, Ernst-Otto-Fischer-Strasse 1, Technical University of Munich, 85747 Garching, Germany
[b] Sustainable Materials Characterization, Van 't Hoff Institute for Molecular Sciences (HIMS), University of Amsterdam, Science Park 904, 1098 XH Amsterdam, the Netherlands
[c] Materials Chemistry, Zernike Institute for Advanced Materials, Faculty of Science and Engineering, University of Groningen, Nijenborgh 4, 9747 AG Groningen, the Netherlands
[d] Clariant Produkte (Deutschland) GmbH – Heufeld, Waldheimer Str. 15, 83052 Bruckmühl Heufeld, Germany[2]

ARTICLE INFO

Article history:
Received 21 August 2020
Revised 14 November 2020
Accepted 20 December 2020
Available online 29 December 2020

Keywords:
Chromite
Spinel
Copper aluminate
Characterisation
XAS
Hydrogenation
Mechanism

ABSTRACT

Copper aluminate spinel ($CuO{\cdot}CuAl_2O_4$) is the favoured Cr-free substitute for the copper chromite catalyst ($CuO{\cdot}CuCr_2O_4$) in the industrial hydrogenation of aldehydes. New insights in the catalytic mechanism were obtained by systematically studying the structure and activity of these catalysts including effects of manganese as a catalyst component. The hydrogenation of butyraldehyde to butanol was studied as a model reaction and the active structure was characterised using X-ray diffraction, temperature programmed reduction, N_2O chemisorption, EXAFS and XANES, including *in-situ* investigations. The active catalyst is a reduced spinel lattice that is stabilised by protons, with copper metal nanoparticles grown upon its surface. Incorporation of Mn into the spinel lattice has a profound effect on the spinel structure. Mn stabilises the spinel towards reduction of Cu^{II} to Cu^0 by occupation of tetrahedral sites with Mn cations, but also causes decreased catalytic activity. Structural data, combined with the effect on catalysis, indicate a predominantly interface-based reaction mechanism, involving both the spinel and copper nanoparticle surface in protonation and reduction of the aldehyde. The electron reservoir of the metallic copper particles is regenerated by the dissociative adsorption and oxidation of H_2 on the metal surface. The generated protons are stored in the spinel phase, acting as proton reservoir. Cu(I) species located within the spinel and identified by XANES are probably not involved in the catalytic cycle.

1. Introduction

The structure and nature of the active sites of hydrogenation catalysts based on copper has not been the focus of scientific research since the early 2000's, despite previous debate regarding the catalytic mechanism. This subject has recently become relevant again due to the demand for stable, Cr-free industrial catalysts in light of the sunset date for Cr^{VI} in 2017, rendering the established copper chromite Adkins catalyst obsolete [1–4]. This catalyst consists of a copper oxide phase distributed over a copper chromite spinel phase ($CuO{\cdot}CuCr_2O_4$) and exhibits excellent stability and activity [3]. Investigated as early as 1991, copper aluminate spinel based catalysts ($CuO{\cdot}CuAl_2O_4$) offer an analogous structure to the Adkins catalyst, where Cr is replaced by Al in the spinel phase [5–7]. These alternative catalysts often contain other metals as additional components for industrial hydrogenation processes [5,8]. Several examples of manganese as component in copper aluminate catalysts are available in the patent literature, though an explanation of the role that manganese plays in these catalysts is lacking [6,9,10]. Manganese possibly increases the stability of the catalysts (e.g. against acidic impurities), and it is claimed that manganese is a necessary part of the catalyst. Recently, also (non-spinel type) Cu/Zn oxides were reported as interesting alternative to Adkins catalysts for hydrogenolysis reactions [11].

The normal spinel structure, found in copper chromite ($CuCr_2O_4$), contains tetrahedrally coordinated Cu^{II} cations in *A*-sites and

* Corresponding authors at: Materials Chemistry, Zernike Institute for Advanced Materials, Faculty of Science and Engineering, University of Groningen, Nijenborgh 4, 9747 AG Groningen, the Netherlands (M. Tromp) and Department of Chemistry, Inorganic Chemistry, Lichtenbergstrasse 4 and Catalysis Research Center, Ernst-Otto-Fischer-Strasse 1, Technical University of Munich, 85747 Garching, Germany (K. Kohler).
E-mail addresses: moniek.tromp@rug.nl (M. Tromp), klaus.koehler@tum.de (K. Köhler).
[1] These authors contributed equally to this work.
[2] Present address.

https://doi.org/10.1016/j.jcat.2020.12.017
0021-9517/

octahedrally coordinated Cr^{III} cations in *B*-sites, following the general formula:

$$A^{II}_{(tet)}B^{III}_{2(oct)}O_4$$

Copper aluminate spinel ($CuAl_2O_4$) is partially inverse, with Cu^{II} and Al^{III} each found in both tetrahedral and octahedral sites [12]. In manganese aluminate spinel ($MnAl_2O_4$), the degree of inversion is dependent on the method of preparation and oxidative transfer between sites can occur, with Mn^{II} in tetrahedral sites converting to Mn^{III} in octahedral sites and the formation of an Al_2O_3 phase with the displaced Al^{III} [13,14]. Fast redox processes within manganese oxides are considered key for their catalytic activity and Mn is therefore often used as an oxophilic redox promotor and electron scavenger to improve selectivity or activity of metal oxide catalysts [15].

The oxidic precursors require an activation step to become hydrogenation catalysts, involving reduction of the copper species under hydrogen flow at elevated temperature. Hydrogen is thought to penetrate the mixed metal oxide bulk to react with Cu^{II} ions, yielding H^+ and Cu^0 [16,17]. Copper atoms migrate to the surface of the catalyst particle and form hemispherical copper nanoparticles in close contact with the residual bulk spinel [18,19]. The protons remain sequestered in the resulting cation deficient lattice in tetrahedral sites previously occupied by Cu^{2+}, covalently bonded to one lattice oxygen and stabilising the structure in the active state [18,20]. XPS measurements combined with XRD showed Cu^{II} in tetrahedral sites are reduced to Cu^{I} (at 150 °C), which migrate to octahedral sites, and to Cu^0 (at 250 °C), whereas Cu^{II} in octahedral sites are reduced at higher temperature (300 °C) to Cu^0 nanoparticles and Cu^{I}, which remain stabilised in the octahedral sites of the spinel [18,21]. *In-situ* XANES investigations of $CuAl_2O_4$ (formed by impregnation of Al_2O_3 with 5 wt% Cu) showed the final copper oxidation states as 70% Cu^0 and 30% Cu^{I}, in a spinel-like environment [22].

The role of the reduced spinel and the copper nanoparticles in the catalytic mechanism of hydrogenation reactions of C=C and C=O double bonds is the subject of some debate. Three possible mechanisms are described in previous research, in which the different copper species are assigned different roles. The first possible mechanism was championed by Bechara et al. in 1985, where they found the catalytic activity of isoprene and 1,3-pentadiene hydrogenation to correlate with the amount of Cu^{I} in octahedral sites of a copper chromite spinel, as well as with H species occluded in the spinel [23]. Bechara et al. concluded that the oxidisable part of the reduced spinel (surface) was therefore more important than the surface area of the metallic copper and identified the active site as a Cu^{I}-H pair [23]. Hubaut et al. extended this research to the selective 1,2-hydrogenation of α,β-unsaturated aldehyde or ketone to the allylic alcohol [24]. This mechanism requires the catalytic activity to be controlled by the amount of Cu^{I} present in the activated spinel.

The second proposed mechanism identified Cu^0 nanoparticles as the site for hydrogen activation under reaction conditions, similar to Group VIII (Pt, Pd or Ni) metal catalysts, but with higher activation energy [25]. Gudkov et al. reported the dependency of the rate equation for the hydrogenation of butyraldehyde on atomic hydrogen. Dissociatively adsorbed hydrogen was confirmed to participate in the reaction mechanism by isotope studies of irreversible butyraldehyde hydrogenation using adsorbed deuterium, where deuterium/hydrogen exchange rates increased with increasing copper content [25]. The capability of metallic copper to dissociatively adsorb hydrogen was reported to be dependent on particle size and the presence of high index faces (2 1 1), (3 1 1) and (7 5 5) [26,27]. It is expected that a mechanism where the copper nanoparticles supply atomic hydrogen and are the active site for hydrogenation would result in catalytic activity correlating with larger metal surface area, which is affected by both particle size and shape.

The third mechanism, described by Yurieva et al. for the hydrogenation of acetone by a reduced copper chromite spinel catalyst, depends on both the surface of Cu^0 nanoparticles and the bulk spinel lattice [28]. According to the authors, acetone is adsorbed on the surface of the Cu^0, which supplies two electrons to the π* orbital of the carbonyl group, giving the carbon a negative charge. Simultaneously, a proton from the spinel lattice transfers to the oxygen to form an alcohol group. This mechanism then describes the migration of the resulting oxidised Cu^{2+} back into the spinel lattice to occupy a previously vacated cation site, whilst a second proton migrates in the reverse direction to the anionic carbon, allowing the alcohol to desorb from the nanoparticle surface. In this way, the reduced spinel lattice behaves as a Brønsted acid, supplying protons, and the nanoparticle acts as a $Cu^{II} \overset{e^-}{\leftrightarrow} Cu^0$ switch, supplying electrons. However, the migration of copper between the spinel and nanoparticle is likely mass transport limiting to the catalytic rate of reaction, making this aspect of the mechanism debatable.

In order to determine which, if any, of these three mechanisms proposed for the traditional chromate system is most likely to be correct in the contemporary copper aluminate spinel-based catalyst ($CuO{\cdot}CuAl_2O_4$) the structure of the activated copper aluminate was investigated. Detailed insights were obtained by characterising the bulk catalysts using XRD, TPR, XANES and EXAFS after synthesis by co-precipitation and calcination to give the spinel structure, and during and after activation in hydrogen forming the final catalyst. The catalytic performance in the reduction of model substrate butyraldehyde by copper aluminate catalysts with varying copper metal surface area and a pure copper spinel model $CuAl_2O_3$ was studied to deduce structure–activity relationships. In particular, the effect of manganese on the structure and redox properties of copper aluminate spinel-based catalysts, which has not been previously investigated, was used as a tool to probe the active structure. Using a combination of techniques, this work attempts to investigate the role of manganese in structure formation, activation and catalytic behaviour of these industrially relevant catalysts and contribute to the discussion on the reaction mechanism.

2. Materials and methods

2.1. Catalyst synthesis

Copper aluminate ($CuO{\cdot}CuAl_2O_4$) catalysts were synthesised via co-precipitation of the metal nitrates with sodium carbonate. A metal nitrate feed solution (0.6 M $Cu(NO_3)_2{\cdot}3H_2O$, 0.6 M $Al(NO_3)_3{\cdot}9H_2O$ and 0.1 M $Mn(NO_3)_2{\cdot}4H_2O$ in Mn including catalyst synthesis) and Na_2CO_3 (2 M) were co-fed into a precipitation vessel containing warm water (50 °C, stirring at 400 rpm) at a rate of 5 mL/min (0.2 M final Cu concentration). The pH was kept at 6.5 by small adjustments to the rate of addition and the precipitates were aged for 1 h (50 °C). The precipitates were subsequently filtered and washed by re-suspending in deionised water until the spent wash fluid had a conductivity ≤ 0.5 mS. The obtained solids were dried at 120 °C overnight and subsequently calcined at 750 °C for 2 h (2 K/min). Catalysts were then activated under H_2 flow, heating at 1 K/min to 300 °C. The final temperature was then held for 1 h before flushing with argon and allowing to cool.

Pure copper aluminate spinel ($CuAl_2O_4$) was prepared in a similar co-precipitation method as described above, using a modified molar ratio of Cu:Al = 1:2. The calcination step was also modified to 800 °C for 2 h (5 K/min). Residual CuO was removed using sat-

urated $(NH_4)_2CO_3$ solution in an ultrasonic bath for 2 h. Thereafter, the leached spinel was stirred at 50 °C for 30 min, filtered, washed with deionised water and dried at 120 °C overnight.

Elemental Analysis (copper and manganese). The samples were digested by treatment with concentrated acids and the metal contents were analysed by photometry.

2.2. Catalyst activity testing

Catalytic tests. Catalytic hydrogenation was carried out on butyraldehyde as a model compound in a 300 mL stainless steel autoclave (Parr) equipped with a heater and overhead stirrer. The reactor was loaded with butyraldehyde (8 g), hexane (100 mL), and n-dodecane (1.2 g) as a GC internal standard. Before addition of the activated catalyst, the liquid phase was de-gassed using argon (Westfalen, 5.0) for 5 min. The autoclave was pressurized with H_2 (60 bar, Westfalen, 5.0) and subsequently heated to 120 °C. After reaching the desired temperature, stirring was commenced (750 rpm) and the reaction time started. After 1 h, the reaction was quenched by stopping the stirring and cooling with an ice bath to 17 °C, upon which the pressure was released. The liquid-phase composition was determined by gas chromatography.

2.3. Analysis and characterisation

Liquid-phase composition of the batch reaction products was determined by gas chromatography (HP6890 gas chromatograph) equipped with a HP-1 methyl siloxane capillary column (60 m × 0.25 mm × 0.25 mm) and a flame ionisation detector (FID). The oven program started at 40 °C with a hold time of four minutes which was then heated to 280 °C with 30 K/min. Helium was used as a carrier gas with 1.2 mL/min and the chromatograph was set to operate at constant pressure. Characteristic retention times and response factors (f_x) were determined using calibration standards. The relationship between f_x, mass (m) and GC peak integral (A) referenced to the internal standard n-dodecane for component identification and quantification.

Catalysts were characterised by X-ray diffraction (XRD) to determine crystallite size and phase composition, temperature programmed reduction (TPR) for reduction behaviour, N_2O-chemisorption for copper surface areas, and finally X-ray absorption spectroscopy for oxidation state (XANES) and local structure (EXAFS).

XRD. X-ray diffractograms were measured on an X'Pert Pro (PANalytic) with a Bragg-Brentano geometry or a Rigaku desktop X-ray Diffractometer with a Miniflex2 counter detector using Cu K_α radiation in the 2θ range 20-70° and step size of 0.01° 2θ. *In-situ* XRD was performed on an X'Pert Pro PW 3040/60 by PANalytical with Bragg-Brentano geometry and Cu K_α radiation (λ = 1.54 Å, 45 kV, 40 mA). The instrument was equipped with a Ni-K_β filter and a solid state detector (X'Celerator). Scanning range was 5–70° 2θ with a step size of 0.017°. The *in-situ* measurements were conducted in a HTK 1200 sample chamber by Anton Parr on a special sample holder equipped with heating. Reduction gas (5% H_2 in N_2) was mixed with Bronkhorst MFCs from the pure gases to obtain a flow of 10 mL/min. Heating rates were set to 2 K/min and samples were allowed to equilibrate after reaching the desired temperatures for 15 min.

Temperature programmed reduction experiments were conducted on a Micromeritics AutoChem 2910. 20 mg of the sample to be analyzed were fixed in the quartz reactor (Ø= 9 mm) with quartz wool. To account for effects such as varying storage time or air humidity, samples were pre-dried and flushed with helium prior to reduction at 120 °C (10 K/min) for 30 min in helium (15 mL/min). After cooling back to room temperature, the cooling trap was equipped with a LN_2/isopropanol cooling bath before the TPR experiments were started. Heating rate was set to 10 K/min with 75 mL/min 2.5% H_2 in argon. TPR experiments were concluded usually at 600 °C and never exceeded 800 °C to avoid damage on the equipment. Removal of hydrogen from the reduction gas was observed with a thermal conductivity detector (TCD) detector. By calibrating the TCD integral of the TPR measurement with hydrogen consumption of a known quantity of pure CuO (see SI Fig. 1), the degree of reduction was calculated by relating hydrogen consumption stoichiometrically to copper content in the catalyst. For this calculation it was assumed that Cu^{II} is completely reduced to Cu^0, as shown in Eq. (2):

$$Cu^{II}O + H_2 \rightarrow Cu^0 + H_2O \quad (2)$$

N_2O chemisorption. Surface area of metallic copper was determined with the N_2O pulse chemisorption method (N_2O gas purity 99.5%, Westfalen) on a Micromeritics AutoChem 2910. The loop volume was calibrated with nitrogen gas as well as the pulse size for complete conversion with the aid of manual injections. Prior to chemisorption, 200 mg of the sample were fixed in the U-tube quartz reactor and subsequently flushed with helium, followed by the activation procedure described above for the catalysts with pre-drying (120 °C, 30 min, 10 K/min). Flows were adjusted to 20 mL/min to account for the reduced amount of catalyst. After activation, the cool trap was supplied with liquid nitrogen. It was verified that flowing nitrogen, product of copper oxidation with nitrous oxide, was not affected and only leftover N_2O was removed by the cooling trap. Via the TCD-integrals calibrated with pure CuO, a stoichiometric factor of two and a surface density of copper of $1.47 \cdot 10^{-19}$ m^{-2} were determined. The relative error of the copper surface area determination was estimated to be ±2%.

In situ-IR with CO chemisorption. For the infrared spectroscopic measurements, a FTS-175 by BioRad was used. A self-made gas cell with a tablet holder as well as heating unit were used. A 2416 by Eurotherm was used as a controller for heating. Gas supplies were connected to the cell with Swagelok tubing. Helium, 1% CO in He and hydrogen gas for the reduction of catalyst tablets were connected and steered by Bronkhorst mass flow controllers. Catalysts were pressed into self-supporting tablets for measurements. After closing of the cell, it was put into the IR spectrometer and connected to the gas supply. The IR was then flushed with N_2 for at least 20 min prior to the first measurement. Activation/treatment procedures were set at 5 mL/min gas flows with heating rates of 1 K/min. After activation, the catalyst tablets were cooled to room temperature in helium before CO-adsorption was begun with varying measurement intervals.

XAS. X-ray absorption spectroscopy experiments were carried out at several beamlines at Diamond Light Source (UK). Measurements Mn K-edge (6539 eV) were carried out at the B18 beamline, using a Si(111) monochromator with Pt coated optics and harmonic rejection and argon filled ion chambers. A Mn^0 foil spectrum was simultaneously obtained with each measurement for energy calibration. However, due to severe oxidation a MnO_2 spectrum was used to determine the amplitude correction. Samples were prepared by diluting the oxidic and reduced catalysts in boron nitride and mixing to homogeneity before pressing into pellets (catalyst depth of approximately 1 unit edge step). The reduced catalyst pellets were sealed in an airtight cell with polyimide (Kapton) film windows before placing in the beam. XANES and EXAFS spectra were collected up to k = 12 in transmission and fluorescence mode.

In-operando measurements at the Cu K-edge (8979 eV) during catalyst reduction were carried out at the I20 beamline, using a Si(111) monochromator with Rh coated optics and harmonic rejection mirrors. A Cu^0 foil spectrum was obtained before measurements were carried out for energy calibration and to deter-

mine the amplitude correction. Samples were prepared by diluting the oxidic catalyst in boron nitride and mixing to homogeneity. The material was pressed into pellets and pushed through a metal sieve. Material of a 125–250 μm diameter sieve fraction was transferred to a quartz capillary flow cell (OD 3 mm, wall thickness 0.05 mm) and held in place with quartz wool (catalyst depth of approximately 1 unit edge step). A thermocouple was placed inside the quartz capillary, which was mounted above a hot air blower and attached to a gas flow controller. Hydrogen gas was then flowed through the capillary (15 mL/min) and temperature was ramped to 300 °C (1 K/min). XANES and EXAFS spectra were collected continuously up to k = 16 in transmission mode, with a 26 °C temperature change during each spectrum. The final temperature was then held for 1 h before allowing the system to cool rapidly under He flow (15 mL/min).

XANES. X-ray absorption near edge structure measurements were processed in Athena (Demeter 0.9.25, using Ifeffit 1.2.12) for background subtraction and normalisation [29]. A Linear Combination Fit (LCF) of the experimental data was carried out with standard reference spectra (Cu0 foil, Cu_2O, CuO, $CuAl_2O_4$). The weighting of the fitting standards was forced to sum to 1 and the fits were evaluated with an *R*-factor (SI Equation 1) and reduced χ^2. These values and the accompanying linear combination fits are shown in the supporting information (SI Table 1 and SI Fig. 3)

EXAFS. Extended x-ray absorption fine structure measurements were processed in Artemis (Demeter 0.9.25, using Ifeffit 1.2.12) for summation of FEFF computed scattering paths and evaluation of the EXAFS equation (SI Equation (2)) for each path. Scattering paths were generated by FEFF calculations using CIF input files of Cu^0, MnO_2 and $MnAl_2O_4$ (modified to remove positions of multiple occupancy) [30–32]. EXAFS fitting of the experimental data (see Supporting Information, SI Table 3 and 4 for fit details) allowed estimation of the average coordination number (*n*) of the first Cu-Cu scattering shell. This is possible because the amplitude of oscillations in k-space that result in the first peak after Fourier transformation to R-space is proportional to the average number of neighbouring atoms in the first coordination shell. Nanoparticle diameters (*D*) and numbers of atoms (*N*) were in turn estimated from *n* using SI Equation 3 (correlation plot shown in SI Fig. 4), following the method developed by Beale and Weckhuysen [33]. The relationship between *n* and nanoparticle size becomes stronger with fewer numbers of atoms, where a greater proportion of the atoms are undercoordinated at the surface and n decreases rapidly.

3. Results

A series of catalysts with including manganese were prepared and compared to the $CuO{\cdot}CuAl_2O_4$ benchmark catalyst. The catalysts were synthesised via controlled co-precipitation in sodium carbonate solutions (with or without addition of manganese). After separation and drying, thermal treatment at 750 °C was necessary for the formation of the spinel structure. Additional catalysts were prepared for comparison in the activity study: Pure ("stoichiometric") copper aluminate spinel ($CuAl_2O_4$; without additional CuO) and $CuO{\cdot}CuAl_2O_4$ catalysts with varying copper metal surface area were obtained by variation of synthesis parameters. The catalytic performance relative to surface area (reported below) demonstrated substantial and complex differences due to the inclusion of Mn. The structures of the (2, 4 and 6 wt%) Mn containing $CuO{\cdot}CuAl_2O_4$ catalysts were therefore studied in detail in comparison to the (0 wt% Mn) benchmark $CuO{\cdot}CuAl_2O_4$ catalyst as oxidic pre-catalysts, and during and after activation by reduction with hydrogen.

3.1. Catalytic activity as function of structure, copper dispersion and manganese content

To explore the catalytic activity of the spinel type $CuO{\cdot}CuAl_2O_4$ catalysts, the batch liquid-phase hydrogenation of butyraldehyde was used as a model reaction. The reaction was performed in an autoclave at 120 °C and 60 bar hydrogen pressure. Before the reaction, the oxidic pre-catalysts were activated in hydrogen at 300 °C for one hour. The yield of butanol is represented as a function of copper nanoparticle surface area in Fig. 1. Two series of $CuO{\cdot}CuAl_2O_4$ catalysts were measured. In the first series (blue ■), copper nanoparticle surface area was varied by modifying the synthesis conditions, see Section 3.2. In the second series (black ▲), nanoparticle surface area was kept constant with increasing Mn content from 0% to 6. In the first series, a linear correlation of activity with nanoparticle surface area is observed. However, presence of 6 wt% Mn results in significantly lower activity (~48% yield) than the Mn free catalyst (~67% yield) with similar copper surface area (~15 m^2/g). In the second series, the yield likewise decreases with increasing manganese content, from 56% at 0 wt% Mn to a minimum of 21% yield at 4 wt% Mn with a slight recovery to 29% yield at 6 wt% Mn. However, while the butanol yield undergoes drastic changes, copper surface area hovers around 9 m^2/g, regardless of manganese content. As the activity of catalysts containing Mn is shown not to correlate to Cu^0 metal surface area, another factor may be expected also to control catalyst activity. The inclusion of manganese therefore offers a possible additional tool to investigate the active state. Finally, despite exhibiting the lowest metallic copper surface area (6.4 m^2/g), the pure spinel phase $CuAl_2O_4$ (red ●) prepared as model system yields more butanol than almost all other catalysts. This indicates that the spinel itself, as well as the nanoparticle surface, is important in the reaction mechanism.

3.2. The crystalline phases studied by XRD

3.2.1. The oxidic pre-catalysts

Manganese has a strong influence on the phase composition and crystallite size of the oxidic pre-catalysts, as shown by XRD analysis (Fig. 2a and b). Increasing manganese content leads to increased crystallinity of $CuAl_2O_4$ spinel (indicated by ●) and CuO phases, indicated by sharper and more intense diffraction peaks. No additional Mn containing phase is formed, but the spinel phase becomes more pronounced after inclusion of Mn, relative to the Mn free catalyst. It is therefore likely that Mn is incorporated into the $CuAl_2O_4$ phase which exhibits higher crystallinity than the Mn free catalyst. The increased peak intensity at higher Mn doping is also indicative of the growth of both spinel and copper oxide crystallites. Crystallite diameters for both phases were determined by the Scherrer equation (indicated by ■ and ● in Fig. 2b and later also summarised in Table 3). In the Mn free catalyst, crystallites as small as 9.4 nm (CuO) and 7.3 nm ($CuAl_2O_4$) are formed; although the error in spinel particle size determination is large as the diffraction peaks are narrow. At 6 wt% Mn, the crystallite sizes of both phases increase to 16.2 nm (CuO) and 12 nm ($CuAl_2O_4$).

3.2.2. The reduced catalyst and the standard activation procedure

The oxidic pre-catalyst is reduced with H_2 to the active structure, resulting in the formation of Cu^0 nanoparticles on the surface of the spinel. The surface area of these nanoparticles was determined by N_2O pulse chemisorption for each catalyst (indicated by ▼ in Fig. 2b). Despite the changes in oxidic crystallite sizes, the surface area of copper nanoparticles after catalyst activation remains surprisingly constant (~9 m^2/g) with increasing Mn content. To further explore the effect Mn has on the reduction behavior to the active catalyst, TPR, XRD, XANES and EXAFS was carried out.

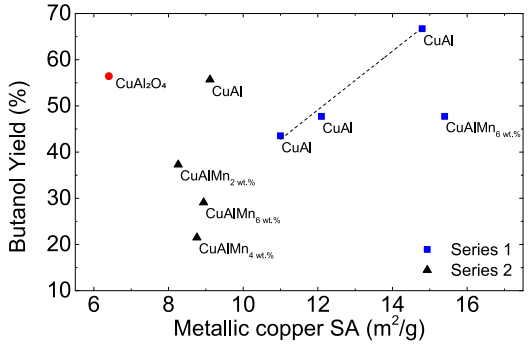

Fig. 1. Catalytic activity in terms of butanol yield (T = 120 °C, p[H_2] = 60 bar, t = 1 h) correlated to Cu^0 nanoparticle surface area. Catalysts containing Mn (black ▲) are compared to pure $CuAl_2O_4$ (red ●) and Mn free $CuO{\cdot}CuAl_2O_4$ (blue ■), synthesised using modified co-precipitation techniques that gave control of copper nanoparticle surface area (for explanation of the series see text).

3.2.3. The influence of manganese studied by TPR

The effect of manganese content on reduction behaviour is very pronounced. TPR studies are shown in Fig. 2c and summarised in Table 3, where the reduction temperature (T_M, given by the TPR peak position) is shifted from 319 °C for Mn free $CuO{\cdot}CuAl_2O_4$ to 257 °C for the 6 wt% Mn containing catalyst. The lower temperature of reduction is not only observed in T_M, but also in the onset of reduction, which is shifted to lower temperatures too and undergoes a faster rate of reaction with Mn presence, as indicated by the steeper slope of the TCD signal. The degree of reduction of Cu^{II} species, determined from the H_2 consumption, assuming stoichiometric Cu^{II} reduction, is presented in Fig. 2d (▲), alongside the reduction temperature (T_M, ●). Up to 97% of total copper in a Mn free $CuO{\cdot}CuAl_2O_4$ catalyst was reduced, whereas 6 wt% Mn decreased the degree of reduction to just 66%. These results suggest that reduction of copper is inhibited in the Mn incorporated spinel. However, the decrease in reduction temperature (T_M) suggests that a certain fraction of Cu^{II} is simultaneously more easily reduced. It is possible that the presence of Mn results in competing effects which account for this contradictory behaviour.

3.2.4. In-situ XRD of catalyst activation by hydrogen reduction

The reduction of an Mn free $CuO{\cdot}CuAl_2O_4$ oxidic catalyst in hydrogen (5% in N_2) was studied further using *in-situ* XRD in order to track the changes in the crystalline phases of the bulk catalyst. The results can be seen in Fig. 3a, where copper oxide reflections decrease in intensity below 150 °C, but the XRD pattern does not change substantially. Above 150 °C, metallic copper appears while spinel and copper oxide reflections remain visible. At 200 °C all crystalline CuO is reduced and metallic copper dominates the diffractogram. At temperatures > 200 °C the spinel peaks shift to higher angles but remain present up to 600 °C. The shift of the pure spinel ($CuAl_2O_4$) reflexes to higher angles is described by Plyasova et al. to be indicative of a contraction of the spinel unit cell caused by reduction of the spinel phase itself [18]. Reduction of pure $CuAl_2O_4$ at 300 °C is known to yield metallic copper and a cation deficient spinel phase, into which protons are incorporated that offset the lost positive charge. Intermediate Cu^I species, Cu_2O and $CuAlO_2$, are also known to form [22,34]. The contraction of the spinel lattice is therefore likely due to the replacement of large Cu^{II} ions by much smaller protons.

For comparison with the Mn free catalyst, 6 wt% Mn-$CuO{\cdot}CuAl_2O_4$ was activated by reduction in hydrogen at 300 °C and also studied using XRD (see Fig. 3b). The CuO reflections are similarly absent in the reduced Mn containing catalyst pattern (grey line), but unlike the Mn free $CuO{\cdot}CuAl_2O_4$, the spinel phase remains distinctive alongside sharp metallic copper peaks. One fur-

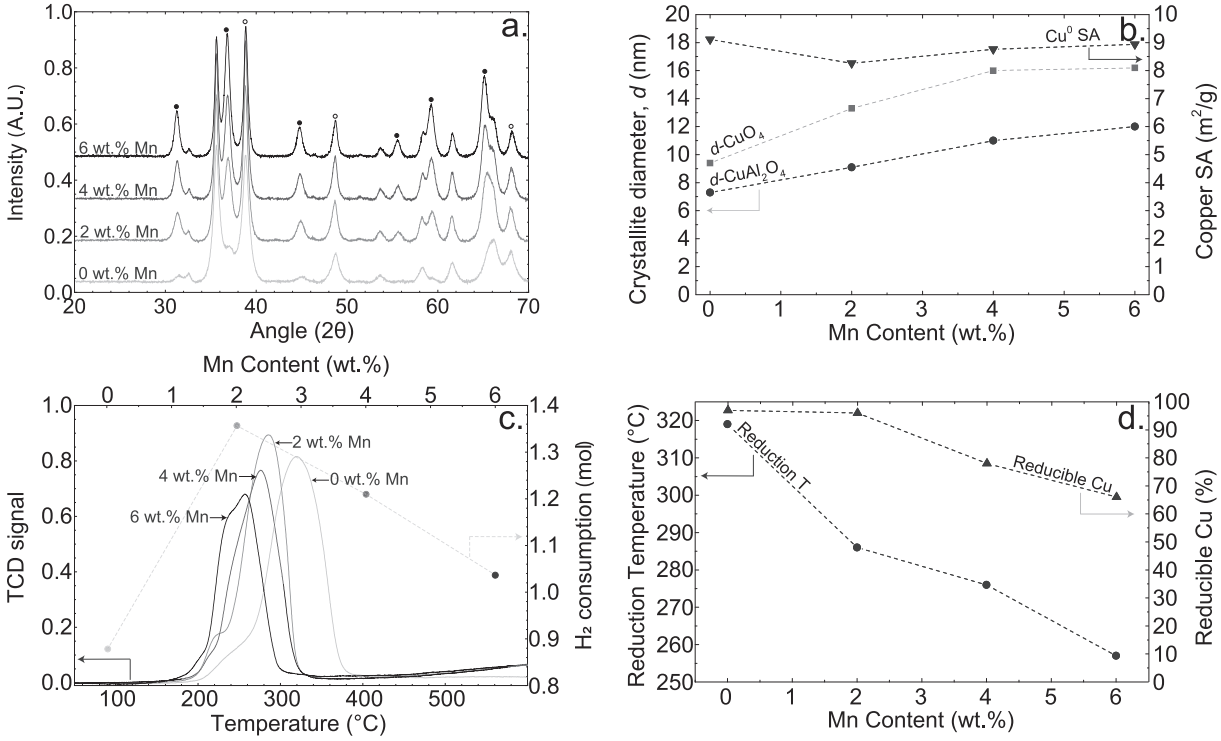

Fig. 2. XRD patterns of oxidic $CuO{\cdot}CuAl_2O_4$ pre-catalysts with increasing Mn wt.%, diffraction peaks due to spinel marked with • (a). CuO and $CuAl_2O_4$ particle diameter calculated with the Scherrer equation from the XRD patterns of pre-catalysts (left axis, b) vs copper nanoparticle surface area of the reduced catalysts (right axis, b; relative error Cu^0 SA: ±2%). TPR profiles of catalysts with increasing Mn wt.% (left axis, c), H_2 consumption, calculated from the TCD peak integral using SI Fig. 1 (right axis, c). Reduction temperature (T_M, left axis, d) vs reducible Cu for catalysts with increasing Mn content (right axis, d).

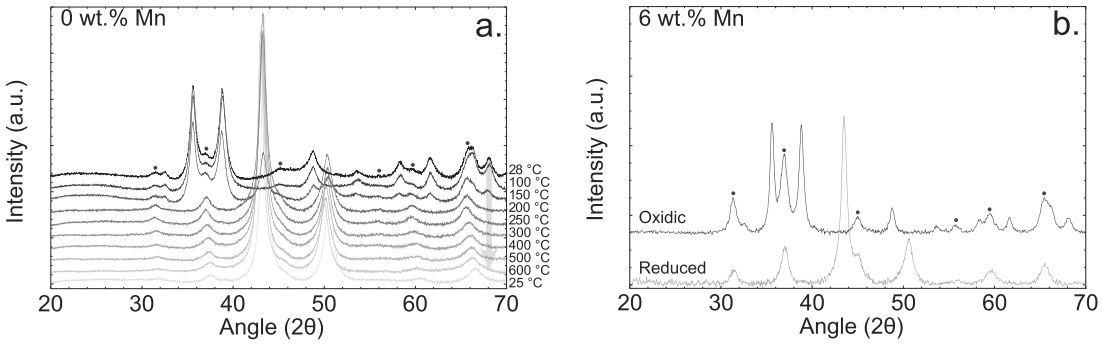

Fig. 3. In-situ XRD measurement of $CuO{\cdot}CuAl_2O_4$ catalyst during activation under hydrogen with increasing temperature from shown dark to light and indicated by the grey arrow (a). Ex-situ XRD measurement of 6 wt% Mn containing $CuO{\cdot}CuAl_2O_4$ catalyst before (black line) and after activation (grey line) in hydrogen at 300 °C (b). Spinel peaks retained after reduction are indicated with black dots (●).

ther essential difference is observed: the spinel peaks are not shifted compared to the oxidic pattern (black line), indicating that the spinel phase with Mn does not undergo a lattice contraction. The absence of a lattice contraction suggests that less Cu^{II} is reduced and removed from the Mn containing spinel phase than in the Mn free $CuO{\cdot}CuAl_2O_4$. The reduced lattice seems to be stabilised by the presence of Mn.

3.3. XANES study on the reduction and the reduced catalyst

3.3.1. In-situ Cu K-edge XANES of catalyst activation and quantification of reduced species

Since XRD only probes crystalline phases, the reduction was studied using *in-situ* XAS to investigate the bulk catalyst, including possible amorphous phases. The Cu K-edge XANES spectra of the Mn free $CuO{\cdot}CuAl_2O_4$ can be seen in Fig. 4a, where the oxidic $CuO{\cdot}CuAl_2O_4$ (black line) exhibits the 1 s → 4p transition at an edge position of 8983.8 eV, (edge position is defined as the maximum point of the first derivative) which lies closer to the edge positions of pure CuO than $CuAl_2O_4$ (8983.5 eV and 8986.6 eV respectively, shown in SI Fig. 2). A weak pre-edge at 8976.5 eV is due to the 1 s → 3d transition, forbidden by dipole selection rules, but observed due to 3d/4p orbital mixing [35,36]. This dipole-forbidden transition is characteristic of Cu^{II} and is not observed in Cu^{I} due to its closed shell d^{10} configuration [37]. Below 200 °C the peak intensity of the white line and oscillations of the multiple scattering region dampen slightly, but the edge position does not change. The reduction of Cu^{II} in the oxidic catalyst occurs between 200 °C and 250 °C, as indicated by the edge shift from 8983.8 eV to 8979 eV, the disappearance of the weak pre-edge feature at 8976.5 eV and the change in oscillations in the multiple scattering region above the edge. At higher temperatures (>300 °C), the catalyst is reduced, with no further spectral changes observed by XAS.

Linear combination fitting of the oxidic and reduced catalysts gives more detailed information on the relative contributions to the observed spectra by different copper species. The Mn free $CuO{\cdot}CuAl_2O_4$ is compared to the 6 wt% Mn-catalyst in Fig. 4b with contributions of reference components ($Cu^{II}O$, $Cu^{II}Al_2O_4$, Cu^{I}_2O and Cu^0, see SI Fig. 3 for fitted spectra) quantified by linear combination fitting of XANES data. Before reduction, the oxidic catalysts are shown to contain Cu^{II} in $CuAl_2O_4$ spinel and CuO species only, with no Cu^{I} contributions to the observed spectra at all. However, the percentage of Cu^{II} in the Mn containing pre-catalyst is higher in the spinel phase than in CuO (58:42%), compared to the Mn free catalyst (51:49%). After reduction, Cu^{II} is almost completely removed from both CuO and $CuAl_2O_4$ phases in the Mn free catalyst, whereas 21% of copper is retained as Cu^{II} in the Mn containing $CuAl_2O_4$ spinel. This results in 70% of copper species forming Cu^0 in the Mn free catalyst, but only 50% Cu^0 when 6% Mn is present. The XANES analysis therefore definitively shows that Mn presence results in greater retention of Cu^{II} in spinel and lower reduction to Cu^0.

3.3.2. Nature of Mn in the pre-catalyst and the active catalyst by Mn K-edge XANES

To assess the role of Mn in the structure, the oxidation state and local coordination of Mn within the catalyst was also investigated using XAS. The XANES of the oxidic and reduced catalysts are shown in Fig. 5a, alongside three manganese oxide references, with the pre-edge feature A and edge features labelled $B_{1/2}$, and the white line feature C. The pre-edge feature A is due to the 1 s → 3d transition and becomes sharper and more intense for non-centro-symmetrically coordinated Mn, for example in tetrahedral sites [38]. The pre-edge feature is sharper in the catalyst XANES spectrum than the octahedrally coordinated manganese oxide reference spectra, indicating that the catalyst contains Mn in tetrahedral sites. Comparison with literature examples of Mn K-edge XANES analysis suggests that the reduced catalyst corresponds to a $MnAl_2O_4$ spinel, identified by the features A-C which are characteristic of Mn spinel structures [13]. The feature labelled $B_{1/2}$ are therefore attributed to the symmetry allowed 1 s → 3p transition, which is divided over two peaks due to the distribution of Mn over two sites in the spinel lattice [39].

The first derivative is shown in Fig. 5b, from which the first peak (B_1) after the pre-edge (A) gives the edge energy E. The K-edge energy shifts are calculated from E-E_0 (where E_0 = 6539 eV) are listed in Table 1, with the corresponding oxidation state of Mn for each compound. The oxidic Mn containing catalyst has an edge shift of 7.7 eV, indicating an oxidation state between 2 and 3, which does not change after reduction to the activated catalyst. However, although all features A-C are present in the reduced catalyst, the shape of the XANES does undergo a change, with a shift in the position and size of feature C. Although the energy shift of the oxidic catalyst is not higher than the reduced catalyst, based on the position of feature B_1, the differences in the spectrum at higher energy indicates contributions from Mn in a higher oxidation state. Linear combination fitting, shown in Fig. 5c, of standard components to the oxidic 6 wt% Mn - catalyst data resolves two 50:50 contributions of $MnAl_2O_4$ spinel and $Mn^{IV}O_2$ to the measured XANES spectrum.

3.4. EXAFS investigations

3.4.1. Nature and role of the Mn

EXAFS fitting was carried out in order to confirm the $MnAl_2O_4$ structure identified in the activated catalyst. Fig. 6 shows the k^2-weighted Mn K edge EXAFS data of the 6 wt% Mn - catalyst in k-

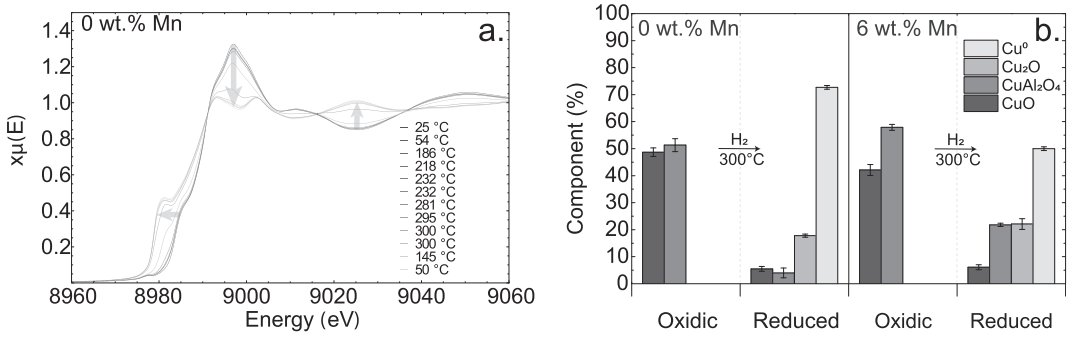

Fig. 4. In-situ Cu K-edge XANES (8979 eV) measurement of $CuO{\cdot}CuAl_2O_4$ catalyst during activation under hydrogen with increasing temperature from shown dark to light and indicated by grey arrows (a). Summary of linear combination fitting (LCF) of XANES measured before and after reduction of Mn free and Mn containing $CuO{\cdot}CuAl_2O_4$ catalysts (b). LCF carried out using standard components: CuO, $CuAl_2O_4$, Cu_2O and Cu^0 metal. See SI Fig. 3. for spectral fits.

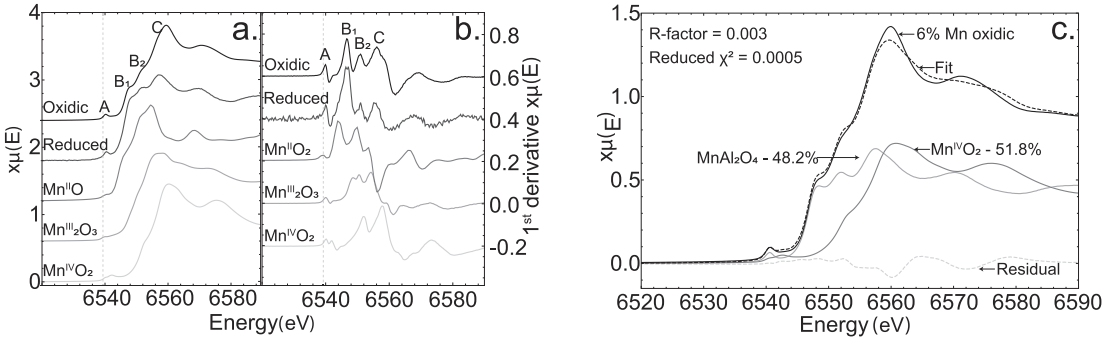

Fig. 5. Mn K-edge XANES (6539 eV) measurement of $CuO{\cdot}CuAl_2O_4$ catalyst with 6% Mn before and after reduction, with edge features labelled A-C, E_0 = 6539 eV shown by the dotted gray line and several manganese oxide structures included for reference (a). First derivative of the Mn K-edge XANES, where the first peak (B_1) after the pre-edge (A) gives the edge energy E (b). Linear combination fitting (LCF) of $Mn^{IV}O_2$ and $Mn^{II/III}Al_2O_4$ spinel standards to the oxidic Mn containing catalyst (c).

Table 1
Energy shift values and corresponding Mn oxidation state [39].

Mn compound	Energy shift E-E_0 (eV)	Mn mean oxidation state
CuAl 6 wt% Mn *oxidic*	7.7	2.5 (+4)
CuAl 6 wt% Mn *reduced*	7.7	2.5
$Mn^{II}O$	5.3	2
$Mn^{III}_2O_3$	8.9	3
$Mn^{IV}O_2$	12.7	4

space (Fig. 6a) and the corresponding k^2-weighted Fourier transformation to R-space (Fig. 6b). The oscillations of the reduced catalyst show a shift to lower wavenumbers which is more pronounced at higher k and the number of contributions also increases. In R-space, the reduced catalyst results in a first shell peak of lower amplitude than the oxidic catalyst, as well as changes is the second shell. The fits for both the oxidic and reduced 6 wt% Mn - catalyst are indicated by the dotted lines in Fig. 6 and the scattering paths and parameters used to generate the fits are summarised in Table 2. The fit to the oxidic catalyst data was generated using scattering paths from two crystal structures ($MnAl_2O_4$ and MnO_2) each given a 50% weighting, based on the LCF results, resulting in an R-factor of 0.01. The fit of the reduced catalyst was generated using only $MnAl_2O_4$ scattering paths, giving an R-factor of 0.02.

In summary, doping the $CuO{\cdot}CuAl_2O_4$ catalyst with 6 wt% Mn results in incorporation of approximately half the Mn into tetrahedral sites of the spinel lattice with oxidation states between 2 and 3. The remaining Mn is located in octahedral sites, either within the spinel lattice or in MnO_2 type structure, with an oxidation state of 4. Activation results in reduction of the Mn^{IV} to an average oxi-

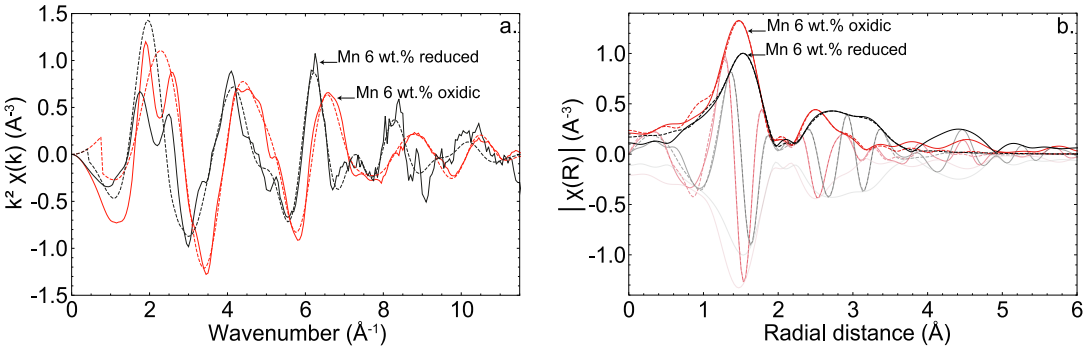

Fig. 6. Experimental k^2-weighted Mn K edge EXAFS (solid lines) and fitting (dotted lines) of oxidic (blue) and reduced (black) 6 wt% Mn - $CuO{\cdot}CuAl_2O_4$ in k-space (a) and after Fourier transformation to R-space (b).

Table 2
EXAFS fitting parameters of oxidic and reduced 6 wt% Mn - $CuO{\cdot}CuAl_2O_4$.

Catalyst	Structure	Shell	n	σ^2 (nm^2)	R (Å)	ΔE_0 (eV)	R-factor
Oxidic	$MnAl_2O_4$	Mn-O_1	4	0.019(5)	2.00(3)	2(2)	0.01
		Mn-Al	12	0.013(4)	3.39(3)		
		Mn-O_2	12	0.016(8)	3.44(3)		
	$Mn^{IV}O_2$	Mn-O_1	6	0.0047(9)	1.887(8)		
		Mn-Mn	2	0.004(2)	2.870(8)		
		Mn-O_2	4	0.03(3)	3.3(2)		
Reduced	$MnAl_2O_4$	Mn-O_1	4	0.007(1)	1.991(7)	0.6(7)	0.02
		Mn-Al	12	0.03(1)	3.39(8)		
		Mn-O_2	12	0.017(5)	3.44(4)		
		Mn-Mn_1	4	0.012(4)	3.54(3)		
		MS: Mn-O_1-Al	48	0.035	3.65(9)		
		MS: Mn-O_1-O_2	48	0.015	4.17(1)		

dation state of 2.5 accompanied by a decrease in the average coordination number (n) from 5 to 4. One explanation is that Mn^{IV} in octahedral sites also migrates to tetrahedral sites within the spinel upon reduction.

3.4.2. Copper nanoparticles in the active catalyst

In order to investigate the copper nanoparticles formed on the reduced catalysts, EXAFS analysis of *in-situ* activated catalysts was carried out. Fig. 7 shows the k^2-weighted Cu K edge EXAFS data of the Mn free $CuO{\cdot}CuAl_2O_4$ and 6 wt% Mn - catalyst in k-space (Fig. 7a) and the corresponding k^2-weighted Fourier transformation to R-space (Fig. 7b). The oscillations of the Mn containing catalyst in k-space are noticeably dampened compared to the Mn free $CuO{\cdot}CuAl_2O_4$. This produces less intense peaks in R-space and is indicative of smaller nanoparticles as a result of Mn presence of the spinel [33]. Assuming hemispherical copper particles, as previously reported by Plyasova et al., with face centered cubic (fcc) structure, the average nanoparticle sizes are quantified Table 3 in terms of diameter and number of atoms [18]. Data fitting to correlate the average coordination number of atoms in the nanoparticles to the size of the nanoparticle is shown in the supporting information (SI Equation 3 and SI Fig. 4). The Mn containing catalyst exhibits smaller nanoparticles, containing just 70 ± 20 atoms with a hemispherical diameter of 1.3 ± 0.2 nm, compared to the Mn free catalyst nanoparticle size of 210 ± 50 atoms and diameter of 2.6 ± 0.3 nm. The presence of 6 wt% Mn therefore results in nanoparticles that are on average half the diameter of those of the Mn free catalyst, with approximately one seventh of the number of atoms.

3.5. Surface vs bulk copper atoms (in-situ infrared spectroscopic experiments)

To further investigate the role of spinel, pure $CuAl_2O_4$ was prepared (Materials and Methods), reduced and analysed *in-situ* with IR-spectroscopy coupled with CO-chemisorption, to probe the outermost catalyst surface. The copper aluminate spinel exposed to CO exhibited the IR bands shown in SI Fig. 5 (descriptions of experiments and assignment of IR bands also in SI) [40]. As expected, an activated spinel consists of Cu^0 as well as of Cu^I/Cu^{II} ions on its surface. Unfortunately, the oxidized species are not distinguishable from each other by this technique. The experiments indicate reduction of $Cu^{I/II}$ ions to metallic copper by CO. The redox reaction with CO at room temperature shows that the surface is highly labile, with multiple oxidation states of copper indicating availability and activity of these species also at the outermost surface.

4. Discussion

As described in the introduction, the mechanism of hydrogenation over copper spinel catalysts is disputed in the literature. Several different possible active species in the reduced spinel have been proposed: a Cu^I species, the Cu^0 nanoparticles, and a combination of both nanoparticles and the spinel support [17,23–25]. Several accessible oxidation states of copper have been identified during reduction of the co-crystallised $CuO{\cdot}CuAl_2O_4$ mixed phase catalysts. Firstly, the CuO phase appears to be directly transformed into crystalline Cu^0, with no intermediate steps or formation of other crystalline species. Previous research on reduction of CuO under industrially relevant conditions also showed that the reduction of CuO to Cu^0 occurs in one step [41,42]. However, CO-probing the pure spinel surface with IR measurement indicates the presence of either Cu^I or Cu^{II} after reduction (SI Fig. 5). Plyasova et al. also suggested that not all spinel copper is reduced completely to Cu^0 but that some Cu^{II} ions are retained within the lattice [43].

The more detailed linear combination fitting of XANES data of reduced catalysts definitively showed the formation of a Cu^I species, likely located within the spinel, as well as significant amounts of Cu^{II} remaining in the reduced Mn containing spinel phase (Fig. 4). The reaction mechanism suggested by Bechara et al. involves Cu^I stabilised in octahedral positions as the active species, as they were able to correlate the amount of Cu^I ions to activity [23]. However, in this research the amount of Cu^I species in the reduced catalysts increases slightly with Mn presence (Fig. 4b), whereas activity was shown to decrease (Fig. 1). This indicates that Cu^I cannot be crucial to the active state, so the research mechanism proposed by Bechara et al. is unlikely to be correct for the catalysts and reaction studied here [23].

The cation deficient reduced spinel lattice forms the bulk of the reduced catalyst, with copper metal nanoparticles growing upon its surface. It is also known that copper nanoparticles can be active sites for the dissociative adsorption of H_2 [25]. Yurieva et al. went further to suggest that metallic copper provides electrons for the hydrogenation, which leads to the expectation that activity must correlate with copper metal surface area [17]. This is not the case, as catalytic activity is reduced by Mn presence whereas the metal surface area remains constant (Fig. 1, Table 3). A mechanism only controlled by dissociative adsorption of H_2 on metallic copper cannot fully explain the observed trend. Furthermore, pure $CuAl_2O_4$ with a smaller copper metal surface area yielded significantly more butanol than expected based on a linear trend between surface area and activity (Fig. 1). This indicates that the reaction mechanism does not only involve the copper metal nanoparticle surface, but is also affected by the structure of the spinel and thus more complex.

Incorporation of Mn into the spinel lattice has a profound effect on the spinel structure. The lattice is stabilised by raising the rela-

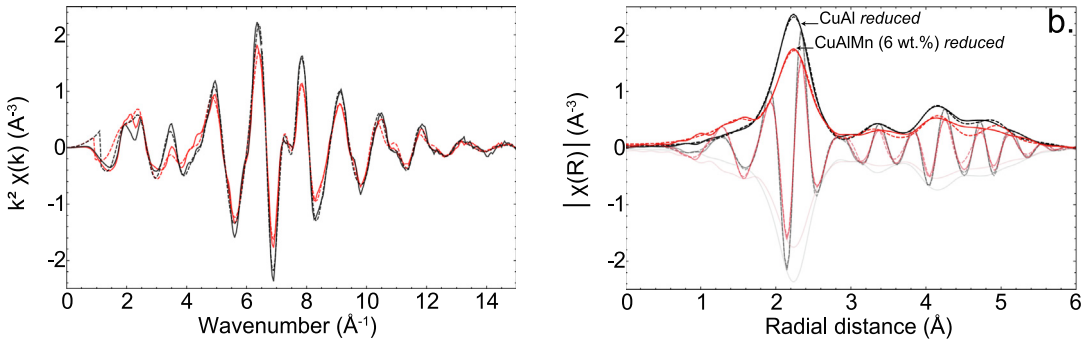

Fig. 7. Experimental k^2-weighted Cu K edge EXAFS (solid lines) and fitting (dotted lines) of Mn free CuO·$CuAl_2O_4$ (black) and 6 wt% Mn containing catalyst (red) in k-space (a) R-space (b).

Table 3
Summary of catalyst characterisation and reduction behaviour.

Mn Content	Butanol yield	Copper metal nanoparticle			Reducible copper[c]	Reduction temperature T_M[c]	Oxidic crystallite diameter[d]	
		Number of atoms[a]	Diameter[a]	SA[b]			CuO	$CuAl_2O_4$
[%]	[%]		[nm]	[m^2/g]	[%]	[°C]	[nm]	[nm]
0	55.7	210(50)	2.6(3)	9.11	97	319	9.4	7.3
2	37.3	*	*	8.26	86	286	13.3	9.1
4	21.5	*	*	8.76	78	276	16	11
6	29.1	70(20)	1.7(2)	8.94	66	257	16.2	12

[a] Determined by EXAFS analysis, calculated errors shown in brackets.
[b] Determined by N_2O pulse chemisorption.
[c] Determined by TPR studies.
[d] Determined using Scherrer equation on XRD powder patterns.
* Not measured.

tive amount of spinel to copper oxide and increasing the spinel crystallite size. This appears to inhibit the reduction of Cu^{II}, causing copper to be retained within the lattice which therefore does not undergo contraction, unlike the Mn free catalyst. At the same time, the reduction of Cu^{II} is facilitated in terms of the lower reduction temperature (T_m, Fig. 2c, Table 3). A variety of mechanisms to explain how Mn simultaneously lowers T_m and prevents a significant percentage of Cu^{II} from being reduced are possible. Mn is a known redox catalyst with several possible oxidation states and could therefore modify the reduction behaviour of the Cu^{II} spinel due to its different redox potential. The spinel structure contains tetrahedral and octahedral cationic sites and Mn is known to occupy both, as either Mn^{II} or Mn^{III} in different types of spinels [14]. XANES and EXAFS measurements of the reduced catalyst showed $Mn^{II/III}$ in predominantly tetrahedral sites, which are known to be vacated by Cu^{II} upon reduction to Cu^0 [18]. The $MnAl_2O_4$ type local structure identified is known to undergo oxidative transfer of Mn^{II} in tetrahedral sites to Mn^{III} in octahedral sites under certain conditions, which are not reduced under 800 °C in 5% H_2/Ar [14,44]. It is therefore possible that Mn^{II}, in tetrahedral sites, could act as an electronic promoter within the spinel, increasing the availability of electrons to Cu^{II} and resulting in a lower temperature of copper reduction.

The decrease in reducible copper could be explained by two further effects in the Mn containing catalyst. The simple increase in crystallite size could result in pathways to the spinel surface that are simply too long for copper to migrate. In addition, blocking of Cu migration pathways by $Mn^{II/III}$ ions incorporated into tetrahedral sites of the spinel structure is also possible. It is considered likely that a combination of all three mechanisms is at play. A lowered redox potential gives rise to a spinel more active towards reduction and accounts for the earlier onset and lower temperature of Cu^{II} reduction in Mn containing catalysts. However, inhibited migration due to larger distances and blocking of pathways could account for the large fractions of Cu^{II} that are not reduced in the manganese containing spinel.

Yurieva et al. championed an interfacial reaction mechanism where protons are supplied by the lattice and electrons are supplied by Cu^0 for the reduction of the reactant molecules, after which the resulting Cu^{II} ions migrate back into the lattice [17]. This type of mechanism, involving the redox reaction of $Cu^{II} \overset{e^-}{\leftrightarrow} Cu^0$, requires access to multiple copper oxidation states in the activated catalysts, which we have shown to be the case. However, in order for this mechanism to be catalytically relevant, unrealistically high rates of ion migration in and out of the lattice would be required per cycle. We therefore propose a modified mechanism: a predominantly interface-based reaction mechanism, involving both the spinel and copper nanoparticle surface (illustrated in Fig. 8). In this mechanism, the electron reservoir of the metallic copper particle is refreshed by the dissociative adsorption and oxidation of H_2 on the nanoparticle surface. The resulting protons are then stored inside the spinel phase and are able to migrate quickly through the outermost layers of the lattice to active sites on the surface. Besides the lower reduction degree of copper in the manganese containing catalyst, an additional effect of Mn in such a mechanism could be to reduce proton capacity of the lattice due to occupation of cation sites by $Mn^{II/III}$ and non-reduced Cu^{II}, which have been shown to be retained in the spinel by XANES analysis (Figs. 4b and 5). The incorporation of Mn ions in the lattice could also block or influence proton migration pathways through the lattice, slowing the resupply of protons to the active sites on the spinel surface. Both, or either, of these effects could account for the reduced activity of the Mn containing catalyst.

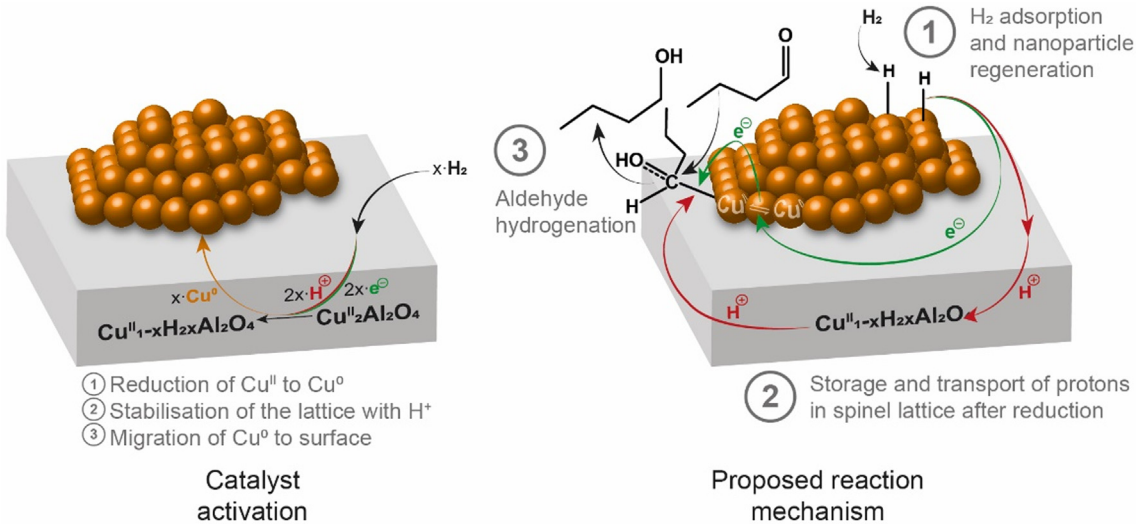

Fig. 8. Visualisation of the active species of reduced copper aluminate spinel catalysts and reaction steps during the hydrogenation of butyraldehyde.

5. Conclusion

Multiple techniques have been used to investigate the structure of the active Mn containing and Mn free $CuO{\cdot}CuAl_2O_4$ catalysts for hydrogenation of butyraldehyde. Mn presence results in a stabilisation of the spinel towards reduction of Cu^{II} to Cu^0 by occupation of tetrahedral sites within the spinel by Mn cations, causing decreased catalytic activity. This has implications regarding the catalytic mechanism and highlights the role of the spinel lattice as a proton reservoir. A modified mechanism is therefore proposed, where the copper nanoparticle acts as a site for H_2 dissociation and supplies electrons and the spinel lattice stores and delivers protons, with the catalytic reaction likely occurring at the interface.

Declaration of Competing Interest

The authors declare that they have no known competing financial interests or personal relationships that could have appeared to influence the work reported in this paper.

Acknowledgements

The authors thank Clariant for funding (to C.D. and K.K.), and NWO and Clariant for funding (NWO LIFT 731.015.407, Launchpad for Innovative Future Technology, PreCiOuS, to M.T. and M.H.). K.K. thanks the University of Amsterdam for an HRSMC (Holland Research School of Molecular Chemistry) fellowship. The authors thank the staff of the I20 and B18 beamlines at Diamond Light Source in Didcot, UK (proposal number SP16558-1) for support and access to their facilities. The authors thank Bas Venderbosch, Jean-Pierre Oudsen and Lukas Wolzak for assistance during synchrotron measurements. The authors would like to thank Ulrike Ammari, Petra Ankenbauer and Bircan Dilki from the microanalytical laboratory at Technical University of Munich for the conduct of elemental analyses.

Appendix A. Supplementary material

Supplementary data to this article can be found online at https://doi.org/10.1016/j.jcat.2020.12.017.

References

[1] Commission Regulation (EU) No 348/2013 of 17 April 2013 amending Annex XIV to Regulation (EC) No 1907/2006 of the European Parliament and of the Council on the Registration, Evaluation, Authorisation and Restriction of Chemicals (REACH), 2013.
[2] H. Adkins, E.E. Burgoyne, H.J. Schneider, The copper—chromium oxide catalyst for hydrogenation, J. Am. Chem. Soc. 72 (1950) 2626–2629.
[3] H. Adkins, R. Connor, The catalytic hydrogenation of organic compounds over copper chromite, J. Am. Chem. Soc. 53 (1931) 1091–1095.
[4] G.M. Kale, Thermal decomposition of $CuCrO_4{\cdot}2CuO{\cdot}2H_2O$ and phase relations in the Cu-Cr-O system, J. Mater. Sci. 30 (1995) 1420–1424.
[5] R.W. Wegman, D.R. Bryant, Catalysts of Cu-Al-third metal for hydrogenation. US Patent 5008235 (1991), to Union Carbide Chemicals and Plastics Technology Corporation (Danbury, CT).
[6] J. Chen, Preparation and use of non-chrome catalysts for Cu/Cr catalyst applications. US Patent 6455464 (2002), to Engelhard Corporation (Iselin, NJ).
[7] M.M. Villaverde, N.M. Bertero, T.F. Garetto, A.J. Marchi, Selective liquid-phase hydrogenation of furfural to furfuryl alcohol over Cu-based catalysts, Catal. Today 213 (2013) 87–92.
[8] Y. Kadono, Hattori, Yasuyuki, Horio, Masamitsu, Nakamura, Fumihiko, Hydrogenation catalyst precursor, hydrogenation catalyst and production process for alcohols. US Patent 5763353 (1998), to Kao Corporation (Tokyo, JP).
[9] M. Schneider, K. Kochloefl, G. Maletz, Chromium-free catalyst for the hydrogenation of organic compounds. US Patent 5403962 (1995), to Sud-Chemie AG (DE).
[10] M. Paulus, Grossmann, Frank, Wegner, Oliver, EXTRUDED Cu-Al-Mn HYDROGENATION CATALYST. US Patent US20170252727 (2017), to Clariant International Ltd. (Muttenz, CH).
[11] V. Pospelova, J. Aubrecht, O. Kikhtyanin, K. Pacultová, D. Kubička, CuZn Catalysts Superior to Adkins Catalysts for Dimethyl Adipate Hydrogenolysis, ChemCatChem 11 (2019) 2169–2178.
[12] E.C. Marques, R.M. Friedman, D.J. Dahm, The structure of copper aluminate: cation distribution at different temperatures and its implications for Cu/Al_2O_3 catalysts, Appl. Catal. 19 (1985) 387–403.
[13] T.N. Stokes, G.D. Bromiley, G.D. Gatta, N. Rotiroti, N.J. Potts, K. Saunders, Cation distribution and valence in synthetic Al–Mn–O and Fe–Mn–O spinels under varying fO_2 conditions, Mineral. Mag. 82 (2018) 975–992.
[14] J.P. Jacobs, A. Maltha, J.G.H. Reintjes, J. Drimal, V. Ponec, H.H. Brongersma, The surface of catalytically active spinels, J. Catal. 147 (1994) 294–300.
[15] S.B. Kanungo, Physicochemical properties of MnO_2 and $MnO_2{\cdot}CuO$ and their relationship with the catalytic activity for H_2O_2 decomposition and CO oxidation, J. Catal. 58 (1979) 419–435.
[16] D.S. Brands, E.K. Poels, T.A. Krieger, O.V. Makarova, C. Weber, S. Veer, A. Bliek, The relation between reduction temperature and activity in copper catalysed ester hydrogenolysis and methanol synthesis, Catal. Lett. 36 (1996) 175–181.
[17] T.A. Krieger, L.M. Plyasova, L.P. Solovyeva, T.M. Yurieva, O.V. Makarova, The structure of copper chromite activated by hydrogen, Mater. Sci. Forum (1996) 627–632.
[18] L.M. Plyasova, T.M. Yureva, I.Y. Molina, T.A. Kriger, A. Balagurov, L.P. Davydova, V.I. Zaikovskii, G.N. Kustova, V.V. Malakhov, L.S. Dovlitova, Dynamics of structural transformations in the reduction of copper aluminate, Kinet. Catal. 41 (2000) 429–436.
[19] L.M. Plyasova, I.Y. Molina, T.A. Krieger, L.P. Davydova, T.M. Yurieva, Structure transformations of copper chromite under reduction–reoxidation conditions, J. Mol. Catal. A: Chem. 158 (2000) 331–336.

[20] A.A. Khassin, G.N. Kustova, H. Jobic, T.M. Yurieva, Y.A. Chesalov, G.A. Filonenko, L.M. Plyasova, V.N. Parmon, The state of absorbed hydrogen in the structure of reduced copper chromite from the vibration spectra, PCCP 11 (2009) 6090–6097.
[21] R. Bechara, A. Aboukaïs, J.-P. Bonnelle, X-ray photoelectron spectroscopic study of a Cu-Al-O catalyst under H_2 or CO atmospheres, J. Chem. Soc., Faraday Trans. 89 (1993) 1257–1262.
[22] M. Fernández-Garcıa, I. Rodrıguez-Ramos, P. Ferreira-Aparicio, A. Guerrero-Ruiz, Tracking down the reduction behavior of copper-on-alumina catalysts, J. Catal. 178 (1998) 253–263.
[23] R. Bechara, G. Wrobel, M. Daage, J.P. Bonnelle, Selective hydrogenation of dienes on copper chromite catalysts II. Structure-activity relationships and catalytic sites, Appl. Catal. 16 (1985) 15–27.
[24] R. Hubaut, M. Daage, J.P. Bonnelle, Selective hydrogenation on copper chromite catalysts IV. Hydrogenation selectivity for α, β-unsaturated aldehydes and ketones, Appl. Catal. 22 (1986) 231–241.
[25] B.S. Gudkov, V.I. Yakerson, A.N. Subbotin, V.M. Kogan, Dissociative adsorption of hydrogen on copper and the mechanism of butyric aldehyde hydrogenation, Mendeleev Commun. 4 (1994) 143–144.
[26] J. Pritchard, T. Catterick, R.K. Gupta, Infrared spectroscopy of chemisorbed carbon monoxide on copper, Surf. Sci. 53 (1975) 1–20.
[27] F. Boccuzzi, G. Ghiotti, A. Chiorino, Metal-semiconductor interaction: Effect of H_2 chemisorption on the IR transparency of the Cu/ZnO system, Surf. Sci. 183 (1987) L285–L289.
[28] T.M. Yurieva, L.M. Plyasova, O.V. Makarova, T.A. Krieger, Mechanisms for hydrogenation of acetone to isopropanol and of carbon oxides to methanol over copper-containing oxide catalysts, J. Mol. Catal. A: Chem. 113 (1996) 455–468.
[29] B. Ravel, M. Newville, ATHENA, ARTEMIS, HEPHAESTUS: data analysis for X-ray absorption spectroscopy using IFEFFIT, J. Synchrotron Radiat. 12 (2005) 537–541.
[30] H.M. Otte, Lattice parameter determinations with an X-ray spectrogoniometer by the Debye-Scherrer method and the effect of specimen condition, J. Appl. Phys. 32 (1961) 1536–1546.
[31] A.S. John, The crystal structure of manganese dioxide, Phys. Rev. 21 (1923) 389.
[32] E.J. Essene, D.R. Peacor, Crystal chemistry and petrology of coexisting galaxite and jacobsite and other spinel solutions and solvi, Am. Mineral. 68 (1983) 449–455.
[33] A.M. Beale, B.M. Weckhuysen, EXAFS as a tool to interrogate the size and shape of mono and bimetallic catalyst nanoparticles, PCCP 12 (2010) 5562–5574.
[34] V. Patrick, G. Gavalas, Structure and reduction and mixed copper-aluminum oxide, J. Am. Ceram. Soc. 73 (1990) 358–369.
[35] L.S. Kau, D.J. Spira-Solomon, J.E. Penner-Hahn, K.O. Hodgson, E.I. Solomon, X-ray absorption edge determination of the oxidation state and coordination number of copper. Application to the type 3 site in Rhus vernicifera laccase and its reaction with oxygen, J. Am. Chem. Soc. 109 (1987) 6433–6442.
[36] J.-N. Nian, S.-A. Chen, C.-C. Tsai, H. Teng, Structural feature and catalytic performance of Cu species distributed over TiO_2 nanotubes, J. Phys. Chem. B 110 (2006) 25817–25824.
[37] P. Khemthong, P. Photai, N. Grisdanurak, Structural properties of CuO/TiO_2 nanorod in relation to their catalytic activity for simultaneous hydrogen production under solar light, Int. J. Hydrogen Energy 38 (2013) 15992–16001.
[38] M. Belli, A. Scafati, A. Bianconi, S. Mobilio, L. Palladino, A. Reale, E. Burattini, X-ray absorption near edge structures (XANES) in simple and complex Mn compounds, Solid State Commun. 35 (1980) 355–361.
[39] M.F. Bekheet, L. Schlicker, A. Doran, K. Siemensmeyer, A. Gurlo, Ferrimagnetism in manganese-rich gallium and aluminium spinels due to mixed valence Mn^{2+}–Mn^{3+} states, Dalton Trans. 47 (2018) 2727–2738.
[40] R. Hierl, H. Knözinger, H.-P. Urbach, Surface properties and reduction behavior of calcined $CuOAl_2O_3$ and CuO-$NiOAl_2O3$ catalysts, J. Catal. 69 (1981) 475–486.
[41] J.A. Rodriguez, J.Y. Kim, J.C. Hanson, M. Pérez, A.I. Frenkel, Reduction of CuO in H2: in situ time-resolved XRD studies, Catal. Lett. 85 (2003) 247–254.
[42] T.H. Fleisch, G.J. Mains, Reduction of copper oxides by UV radiation and atomic hydrogen studied by XPS, Appl. Surf. Sci. 10 (1982) 51–62.
[43] L.M. Plyasova, L.P. Solovyeva, T.A. Krieger, O.V. Makarova, T.M. Yurieva, The nature of hydrogen stabilization in the reduced copper chromites, J. Mol. Catal. A: Chem. 105 (1996) 61–66.
[44] A. Maltha, H.F. Kist, B. Brunet, J. Ziolkowski, H. Onishi, Y. Iwasawa, V. Ponec, The active sites of manganese- and cobalt-containing catalysts in the selective gas phase reduction of nitrobenzene, J. Catal. 149 (1994) 356–363.